RSC Advances

PAPER

View Article Online
View Journal | View Issue

Cite this: *RSC Adv.*, 2026, **16**, 28366

The production and electrochemical performance analysis of an O3-$NaTi_{0.2}Mn_{0.2}Fe_{0.2}Ni_{0.2}Co_{0.2}O_2$ high-entropy oxide cathode for Na-ion batteries

Ali Topal,[a] Abdul Naveed,[ab] Crispin Hetherington,[c] Rachel Gouttebaron,[d] Sevda Sahinbay *[e] and Serdar Altin *[af]

In this study, we report the suppression of degradative transformations observed in Na-ion batteries by utilizing five different transition-metal cations at a single crystallographic site, which is expected to impart entropy-induced stabilization, resulting in enhanced structural stability. We successfully synthesized phase-pure O3-$NaTi_{0.2}Mn_{0.2}Fe_{0.2}Ni_{0.2}Co_{0.2}O_2$ through a facile solid-state sintering method. In this compound, Co^{3+}, Fe^{3+}, and Ni^{2+} provide charge compensation for capacity, Mn^{4+} acts as a structure former, and Ti^{4+} helps stabilize the overall structure. The synthesized material was successfully characterized using X-ray diffraction (XRD), scanning electron microscopy with energy dispersive X-ray spectroscopy (SEM/EDX), inductively coupled plasma mass spectroscopy (ICP-MS), X-ray photo-electron spectroscopy (XPS), and transmission electron microscopy (TEM). The configurational entropy was calculated to be ~1.6 R, which is consistent with a high-entropy oxide. The material revealed a single phase with $R\bar{3}m$ symmetry, which matches well with the O3-type layered structure. SEM revealed irregular 1–3 μm particles, while EDX mapping confirmed uniform elemental dispersion. ICP provided the composition as $Na_{0.94}(Ti_{0.18}Mn_{0.20}Fe_{0.20}Ni_{0.21}Co_{0.21})O_2$. The XPS analysis showed mixed-valence chemistry for each component (Ti is predominantly Ti^{4+} with minor metallic Ti; Mn is consistent with Mn^{4+}; Fe exhibits Fe^{2+}/Fe^{3+} coexistence; Co exhibits Co^{2+}/Co^{3+} coexistence; and Ni exhibits Ni^{2+}/Ni^{3+} coexistence), which can be explained by a charge compensation mechanism. Transmission electron microscopy and selected area electron diffraction (TEM-SAEED) analysis confirmed the formation of an $R\bar{3}m$ structure, and the interlayer separation was also calculated. The electrochemical properties were systematically evaluated, and the capacity of the cells was found to be 120 mA h g^{-1} at a C/3-rate, which demonstrates the promising potential of this composition for sodium-ion battery applications.

Received 25th March 2026
Accepted 4th May 2026

DOI: 10.1039/d6ra02449a

rsc.li/rsc-advances

1 Introduction

Lithium-ion batteries (LIBs) are the leading technology for energy storage in electric vehicles and portable electronics. However, their long-term scalability is impeded due to limited and unevenly distributed lithium resources, which are largely concentrated in countries such as Chile, Argentina, and Bolivia.[1–3] To overcome these drawbacks, scientific studies have focused on sodium-ion batteries (SIBs). SIBs operate through similar electrochemical principles to LIBS but have the advantages of worldwide distribution, natural abundance and low cost, which make them promising alternatives for large-scale energy-storage systems.[4,5] Numerous studies are being conducted to develop advanced electrode materials for increasing the efficiency of SIBs.

One of the most promising electrode material families for SIBs is layered oxides having a general formula of Na_xTMO_2, where TM is a transition metal. These layered oxides have low cost, facile synthesis, simple structure, high voltage and high specific capacity.[6–8] Unlike Li_xTMO_2 layered oxides, Na_xTMO_2 exhibits diverse phase transitions attributed to different possible stacking sequences, the larger ionic radius of Na^+ and the stronger electrostatic repulsion between adjacent Na^+ ions within the NaO_2 layers.[9] The adopted crystal system and layer stacking depend on the Na content. Sufficiently high Na^+ content ($0.8 < x \leq 1.0$) results in an O3-type stacking with octahedral coordination similar to $LiCoO_2$. Lower Na^+ content

[a]*Physics Department, Inonu University, Battalgazi, Malatya 44280, Turkey. E-mail: serdar.altin@inonu.edu.tr*
[b]*Department of Chemistry, Quaid-i-Azam University, Islamabad 45320, Pakistan*
[c]*Centre for Analysis and Synthesis, Department of Chemistry, Lund University, 22100 Lund, Sweden*
[d]*Synthesis, Irradiation & Analysis of Materials (SIAM) Technological Platform, University of Namur, Rue de Bruxelles 61, Namur 5000, Belgium*
[e]*Physics Engineering Department, Istanbul Technical University, Istanbul 34467, Turkey. E-mail: sahinbays@itu.edu.tr*
[f]*Battery Technology Application and Research Center, Inonu University, Battalgazi, Malatya 44280, Turkey*

with $x = 0.4–0.8$ favors the formation of P2- or P3-type structures with trigonal-prismatic coordination sites.[9] In addition, edge-sharing TMO_6 octahedra containing TMO_2 layers play a crucial role in the formation of the stacking pattern and crystal structure. Thus, it is critical to carefully select the ratios of TMs as well as Na content for structural modulation.

Extensive research was conducted on layered oxides for SIBs containing a single TM, such as $NaCoO_2$, $NaFeO_2$, $NaMnO_2$, $NaCrO_2$, and $NaNiO_2$, which usually suffer from drastic phase transitions and capacity fading during repeated charge–discharge cycles.[10–14] To improve the stability and suppress the phase transition from an O3- to a P3-type lattice, bimetallic oxide synthesis approaches, such as $NaNi_{1/2}Mn_{1/2}O_2$ and further substitution, such as (i) substitution of Mn^{4+} by Ti^{4+}, (ii) simultaneous substitution of Mn^{4+} and Ni^{2+} with Fe^{3+} and (iii) dual substitution of Mn^{4+} and Ni^{2+} with Ti^{4+} and Mg^{2+}/Cu^{2+}, were investigated and better electrochemical properties than that of single TM element in the structure were observed.[15–17] Despite these encouraging results, these materials encountered phase impurities, intra-granular cracking and TM dissolution during cycling.

A recent strategy to synthesize single-phase layered oxides is to maximize configurational entropy. The single-phase layered oxides containing five or more principal elements exhibit high configurational entropy (generally $\geq$ 1.5 R) and are referred to as high entropy oxides (HEO). In high-entropy oxides (HEOs), the value of "1.5 R" is historical and empirical rather than a strict thermodynamic boundary. Empirical work on high-entropy alloys showed that when moving from 4 to 5 equiatomic elements, single-phase solid solutions could more often be obtained; the corresponding ideal configurational entropy is $\approx$1.61 R for 5 equiatomic components. This led to an early definition of "high entropy" as $\Delta S_{mix} \geq$ value for 5 equiatomic elements ($\approx$1.61 R), with "low entropy" $\leq$ that for 2 equiatomic elements ($\approx$0.69 R). Some authors later rounded this to $\Delta S_{mix} \geq$ 1.5 R for high entropy, $\leq$1.0 R for low entropy, and used the in-between range as "medium entropy". These alloy-based criteria were then directly carried over to oxides.[18,19]

Different elements with varying sizes, electronegativities and oxidation states randomly distributed in the entire crystal result in different bonding and complex local structures, which cause excessive distortion in the lattice.[20] Such distortion is expected to impede the movement of neighboring atoms, while high entropy lowers Gibbs free energy change (ΔG) and stabilizes single-phase structures, especially during high-temperature synthesis. This strategy is broadly applicable to layered oxides and rock-salt, spinel, and perovskite-type structures.

In this study, we synthesized single-phase O3-$NaTi_{0.2}Mn_{0.2}Fe_{0.2}Ni_{0.2}Co_{0.2}O_2$ through a facile solid-state sintering method in which Co^{3+}, Fe^{3+}, Ni^{2+} provide charge compensation for capacity, Mn^{4+} serves as a structure former, while Ti^{4+} helps in stabilization of the overall structure.[21] The synthesized HEO was successfully characterized through XRD, SEM/EDX, ICP, XPS and evaluated for sodium ion battery application. The electrochemical properties were investigated using CR2032 cells with Na-metal as the reference electrode in a half-cell configuration, yielding promising results for future applications.

2 Experimental section

2.1 Material synthesis

Na_2CO_3 ($\geq$99.5%), TiO2 ($\geq$99%), MnO_2 (($\geq$99%), Fe_2O_3 (99%), Co_3O_4 (99.5%), and NiO (99%) were used as raw materials without further purification. For the synthesis of $NaTi_{0.2}Mn_{0.2}Fe_{0.2}Ni_{0.2}Co_{0.2}O_2$, first, Na_2CO_3 (0.55 mmol), Mn_2O_3 (0.1 mmol), Fe_2O_3 (0.1 mmol), NiO (0.2 mmol), CoO (0.2 mmol) and TiO_2 (0.2 mmol) were mixed in a mortar for 30 minutes. The prepared material was pressed into pellets with a 1.50 cm diameter using a uniaxial hydraulic press under 60 bar pressure. The pelletized material was heated at 900 °C for 12 h in a Protherm PC442 tube furnace before quenching with liquid nitrogen. The as-prepared pellets were milled again into nanoparticles in isopropyl alcohol for 12 h, and then dried in a glove box for 1 day at room temperature. The synthesis procedure is presented in Scheme 1. To avoid oxidation, the as-synthesized material was transferred and stored in an I-Lab argon glovebox (Inert Technology) with high purity (H_2O, O_2 < 0.1 ppm). Moreover, a 10% excess Na source was used to compensate for Na loss during calcination.

2.2 Characterization

Crystal structure investigation of $NaTi_{0.2}Mn_{0.2}Fe_{0.2}Ni_{0.2}Co_{0.2}O_2$ was conducted *via* X-ray diffraction (XRD) using a Rigaku Rad-B Dmax-2 diffractometer. The data were collected with Cu Kα radiation (λ = 1.5406 Å) across a 2θ range of 3–80° with a step size of 0.02° and a scanning speed of 3° per min. The surface functional groups were characterized by Fourier-transform infrared (FTIR) spectra (400–4000 cm^{-1}) with a Bruker Vertex 70 system equipped with an ATR unit. Raman spectroscopy measurements were conducted on a JASCO NRS-4500 confocal system using a 532 nm laser, a 50× objective, and a 10 s integration period. A LEO EVO 40 SEM operating at 25 kV, coupled with an EDX module for elemental analysis, was utilized for morphological characterization. High-resolution imaging (TEM and HR-TEM) was facilitated by the National Center for High Resolution Electron Microscopy (nCHREM) at Lund University using a 200 kV JEOL JEM-2200FS microscope. Surface chemistry was studied using a Thermo Scientific K-Alpha+ XPS spectrometer (Al Kα monochromated X-ray source, 1486.6 eV). The charge correction was calibrated to the C 1 s peak at 284.8 eV. Bulk composition and stoichiometry were verified using an Agilent 5100 SVDV ICP-OES system. Decomposition of the HEO samples (30–100 mg) was performed in a microwave system using a 4 : 2 : 1 (v/v) mixture of 37% HCl, 65% HNO_3, and H_2O_2. The following temperature profile was employed; a 10 min ramp to 200 °C and a 35 min hold at 35 bar, ending with a cool-down to 50 °C. After this step, the samples were diluted with 15 mL ultrapure water, with a 0.1 mL aliquot prepared for analysis. A PerkinElmer NexION 350X ICP-MS with a Meinhard concentric nebulizer and a nickel triple-cone interface was used to collect data. The helium (He) kinetic energy discrimination mode at 1500 W RF power was utilized to minimize spectral interferences.

2.3 Electrochemical measurements

The HEO electrodes were prepared by mixing the active material, carbon black, and a polyvinylidene fluoride (PVDF) binder with

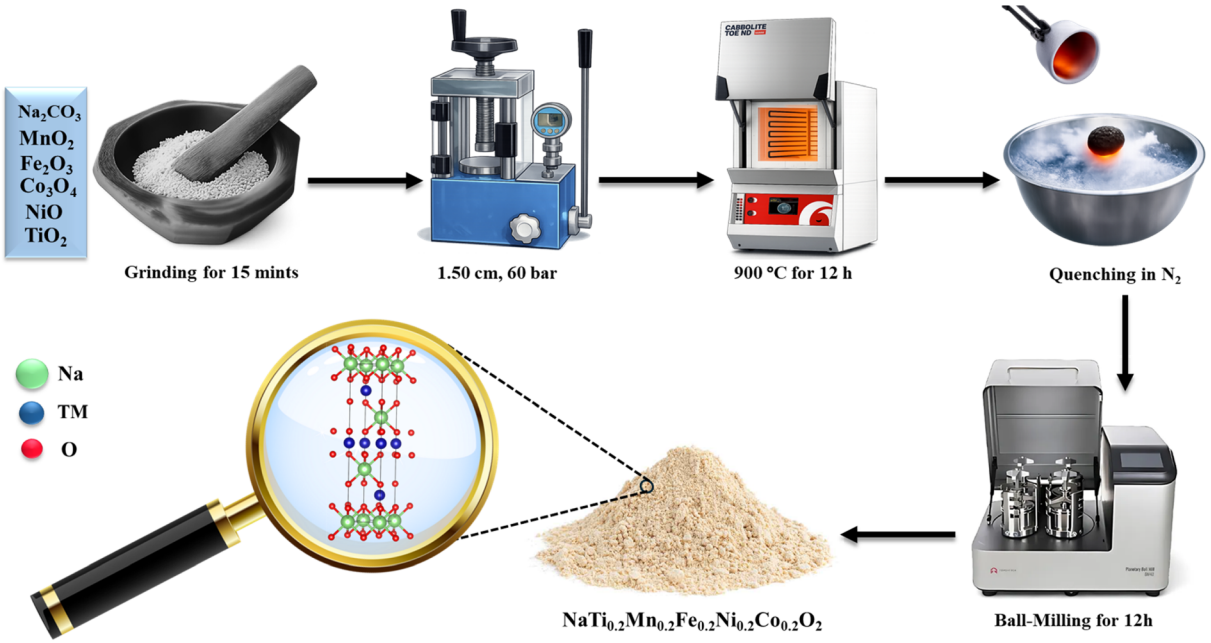

Scheme 1 Synthesis steps of $NaTi_{0.2}Mn_{0.2}Fe_{0.2}Ni_{0.2}Co_{0.2}O_2$.

a weight ratio of 80 : 10 : 10. The slurry was homogenized using a Planetary Centrifugal Mixer (THINKY MIXER ARE-250, non-vacuum) for 30 minutes at 2000 rpm. The mixture was cast onto aluminum foil current collectors and subsequently dried under vacuum at 110 °C for 12 hours to remove residual solvents. CR2032-type coin cells were assembled in a high-purity argon-filled glovebox (H_2O, O_2 < 1 ppm). Sodium metal was used as the counter/reference electrode, separated from the cathode by a glass fiber separator. The electrolyte was prepared by dissolving 1.0 M $NaClO_4$ in a 50/50 v/v ratio of propylene carbonate (PC) and ethylene carbonate (EC). The mass of the active material on the electrodes was kept between 1.8 and 2.6 mg cm^{-2}. The redox characteristics of electrodes in the half-cell configuration were investigated *via* cyclic voltammetry (CV) using an IVIUM Octastat 30 workstation within a voltage window of 1.5–4.3 V at a scan rate of 0.1 mV s^{-1}. A Neware battery tester was utilized for galvanostatic charge–discharge tests at a C/3 rate (1C = 120 mA h g^{-1}) over 100 cycles within the same potential limits. Varying current rates ranging from C/10 to 2C were applied to study rate capabilities. Electrochemical impedance spectroscopy (EIS) measurements were performed using a ZIVE SP1 workstation to determine kinetic parameters and interfacial resistances. Frequencies in the range of 200 kHz to 10 mHz were used with an AC perturbation amplitude of 10 mV. *In situ* EIS measurements were conducted to probe the dynamic evolution of impedance during cycling. Galvanostatic intermittent titration technique (GITT) was used with a sequence of 10 minute current pulses separated by 60 minute relaxation intervals to determine the solid-state diffusion coefficients of sodium ions (Na^+).

3 Results and discussion

3.1 Structural and morphological characterization

The phase stability of HEO compositions is attributed to the high configurational entropy, which is achieved by randomly distributed cations on the same crystallographic site in equimolar ratios. The quantity of this thermodynamic state can be determined by the following standard Boltzmann relationship:[8]

$$\Delta S_{\text{config}} = -R\left[\left(\sum_{i=0}^{M} x_i \ln x_i\right)_{\text{cation-site}} + \left(\sum_{j=0}^{M} x_j \ln x_j\right)_{\text{anion-site}}\right] \quad (1)$$

where R is the universal gas constant. M and N represent the amount of distinct ionic species residing in the cation and anion sublattices, respectively, where x_i and x_j denote their mole fractions. A threshold value of 1.5 R is formally established to characterize a material as "high entropy". Our synthesized material yields a specific entropy of 1.6 R, confirming its high entropy classification. The crystal structure of the as-prepared HEO was evaluated with X-ray diffraction, followed by Rietveld refinement using the GSASII interface.[22] Fig. 1(a) shows the XRD pattern with the Rietveld refinement profile (w_R = 3.4 with GoF = 0.44), confirming the highly crystalline single-phase structure. The crystal structure was identified as an O3-type hexagonal structure with $R\bar{3}m$ symmetry. The lattice parameters are determined as a = 2.9831(1) Å and c = 16.071(1) Å, and a cell volume of 123.9(3) $Å^3$. The lattice parameters obtained in this study demonstrate good agreement with previously reported values for O3-type layered cathodes (a = 2.967 Å, c = 16.009 Å), with minor variations attributed to the specific transition metal composition and doping strategies employed here.[23] The non-proportional change in the lattice parameters can be attributed to the anisotropic nature of the O3-type layered structure. While the a-parameter is primarily governed by the transition metal ionic radii and their intra-layer bonding, the c-parameter is highly sensitive to the electrostatic repulsion between oxygen layers and the shielding effect of sodium ions in the interlayer galleries.

Fig. 1(b) and (c) show a schematic representation of the layered structure, characterized by the alternating stacking of

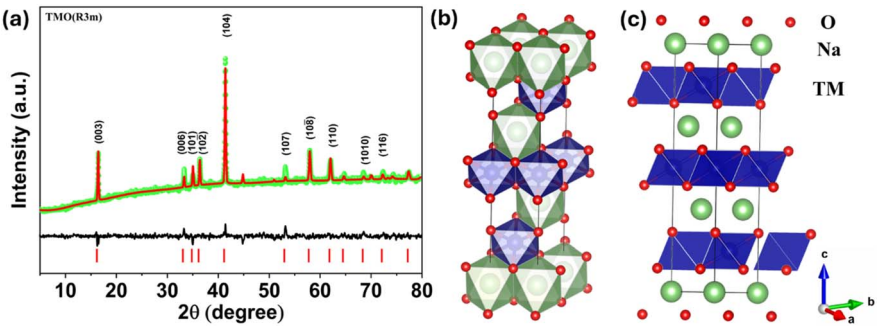

Fig. 1 (a) Rietveld refinement profile of the X-ray diffraction (XRD) pattern for the $NaTi_{0.2}Mn_{0.2}Fe_{0.2}Ni_{0.2}Co_{0.2}O_2$ cathode material. (b) and (c) schematic of the crystal structure, illustrating the well-ordered stacking of transition metal oxide (TMO_6) octahedral slabs and the accommodation of sodium ions within the interlayer diffusion channels.

transition metal oxide slabs and sodium layers. Transition metal cations bonded to six oxygen atoms form the TMO6 octahedral building blocks within the TMO2 sheets. These slabs offer two-dimensional diffusion pathways for Na ions.

The stoichiometry of $NaTi_{0.2}Mn_{0.2}Fe_{0.2}Ni_{0.2}Co_{0.2}O_2$ yields the following oxidation states: Ti^{4+} (0.605 Å), $Mn^{3+/4+}$ (0.645 Å/0.530 Å), Fe^{3+} (0.645 Å, high spin), Ni^{2+} (0.690 Å), and Co^{3+} (0.545 Å, low spin).[24] The calculated *a*-parameter of 2.98 Å represents an expansion in this lattice direction when compared to pristine systems, such as O3-$NaMnO_2$ (2.86 Å).[25] While the presence of larger cations like Ni^{2+} (0.69 Å) and high-spin Fe^{3+} (0.645 Å) contributes to slab thickening in the lattice and this expansion is fundamentally driven by the high-entropy compositional design. The chemical disorder inherent in this multi-element system induces significant local lattice distortions and the associated internal microstrain. From the perspective of defect chemistry, the high configurational entropy stabilizes these local distortions, effectively 'pinning' the lattice and preventing the excessive contraction observed in lower-entropy analogs. This lattice strain energy modifies the potential energy landscape of the slabs, which may also play a role in modulating the Na^+ diffusion pathways.

In addition, the *c*-parameter, representing the interlayer spacing, indicates the contribution of the high-entropy configuration to eliminate the interlayer collapse. This can be attributed to repulsive coulombic interactions between distinct oxygen environments created by disordered cations in the TM layers. Our sample shows structural integrity upon the successful integration of all five metals into a single phase compared with similar multi-element layered oxides, such as the quinary $NaNi_{0.12}Cu_{0.12}Mg_{0.12}Fe_{0.15}Ti_{0.15}Mn_{0.1}O_2$ reported by Zhao *et al.*[21] This structural robustness is characteristic of entropy-stabilized oxides, in which configurational entropy compensates for the enthalpic strain caused by the ionic size mismatch. The coexistence of various ions, such as Ti^{4+}, Mn^{4+}, Fe^{3+}, Ni^{2+}, and Co^{3+}, causes severe lattice distortions within their local environments, attributed to the significant mismatch in ionic radii and valence. Such local distortions lead to anisotropic crystal fields that are substantially different from the uniform environments of standard layered oxides, providing an "anchoring effect" that enhances the stability of the structure and suppresses the Jahn–Teller effect, a common structural deformation observed in Mn-based oxides. In addition, the formation of superstructures through Na ion ordering is prevented by non-homogeneous charge distribution within the transition metal layers. The layer gliding observed during high voltage P2-O2 phase transitions is also prevented due to local strain that pins the TMO_2 slabs.

Fig. S1(a) shows the FTIR pattern of HEO containing five zones. Region A, with low frequency, represents the characteristic vibrations of the MO_6 octahedral framework. The M–O stretching bands in this region are broad envelopes rather than sharp peaks, a characteristic of high-entropy materials due to the diversity of local environments caused by the random distribution of TMs. Regions B and C indicate the presence of carbonate species maintaining surface stability. The broad asymmetric stretching band at 1400–1500 cm^{-1} (Region C) and the minor bending mode (Region B) can be attributed to the formation of a Na_2CO_3 film due to air exposure. However, the weakness of these signals implies that this layer is minimal. The O–H stretching mode at ~3400 cm^{-1} (Region E) and the H–O–H bending mode at ~1640 cm^{-1} (Region D) are ascribed to ambient moisture adsorbed during experimental preparation.

The Raman spectrum in Fig. S1(b) displays characteristic peaks corresponding to the A1g (symmetric stretching of M–O bonds along the *c*-axis) and E_g (vibration of oxygen atoms in the *ab*-plane) modes of the layered $R\bar{3}m$ symmetry.[26] These peaks are significantly broader than those of simple transition metal oxides, which confirms the high-entropy configuration. Random distribution of five different cations (Ti, Mn, Fe, Ni, and Co) with varying ionic radii leads to different bond lengths and bond strengths, resulting in a disordered local environment despite the long-range crystalline order.[26,27]

The SEM images of the surface morphology of our sample are shown in Fig. 2(a–c). The images reveal micrometric particles with irregular geometries ranging from 1 to 3 μm in size. These irregular formations are characteristic of high-temperature solid-state synthesis of O3-type Na-based layered oxides. The particle edges indicate a pseudo-hexagonal or plate-like morphology, confirming crystallinity and preferential growth along the *ab*-plane. All these morphological features are expected to be beneficial during electrochemical cycling. The

well-defined crystal facets and relatively small particle sizes shorten the diffusion pathways for Na^+ ions. In addition, sufficient electrode packing density is maintained by the robust micrometric dimensions.

The chemical uniformity and bulk stoichiometry of our sample were examined by EDX analysis, shown in Fig. S2, confirming the presence of Na, Ti, Mn, Fe, Ni, and Co within the selected area. The atomic percentages of the TMs obtained from the EDX spectrum are very close to the nominal values, ranging between 8.8% and 10.8%, aligning well with the aimed equimolar composition of $NaTi_{0.2}Mn_{0.2}Fe_{0.2}Ni_{0.2}Co_{0.2}O_2$. In addition, 1.06 ratio of Na/TM suggests a slight sodium excess, which can be attributed to the surface passivation layers common in sodium-layered oxides.

Fig. 2(d) shows the elemental color maps for Na, Ti, Mn, Fe, Ni, and Co, indicating a highly uniform distribution of all atoms without any detectable phase segregation or clustering of specific transition metals, which is a common issue in materials containing multiple elements. This observation was further confirmed by elemental mapping at higher magnification, as shown in Fig. S3. This homogeneous elemental distribution supports the successful synthesis of a single-phase solid solution, confirming the incorporation of all the TMs in the crystal lattice at the atomic level. To further verify the stoichiometry and the local homogeneity, we performed ICP-MS measurements on our sample. While EDX provides information on the surface composition, with slightly excess Na due to surface passivation layers, ICP-MS offers a more accurate global elemental ratio. The ICP-MS analysis yielded elemental concentrations of 215 947 ppm for Na, 110 782 ppm for Mn, 111 780 ppm for Fe, 124 312 ppm for Ni, 124 405 ppm for Co, and 85 391 ppm for Ti. The conversion from ppm values to molar ratios

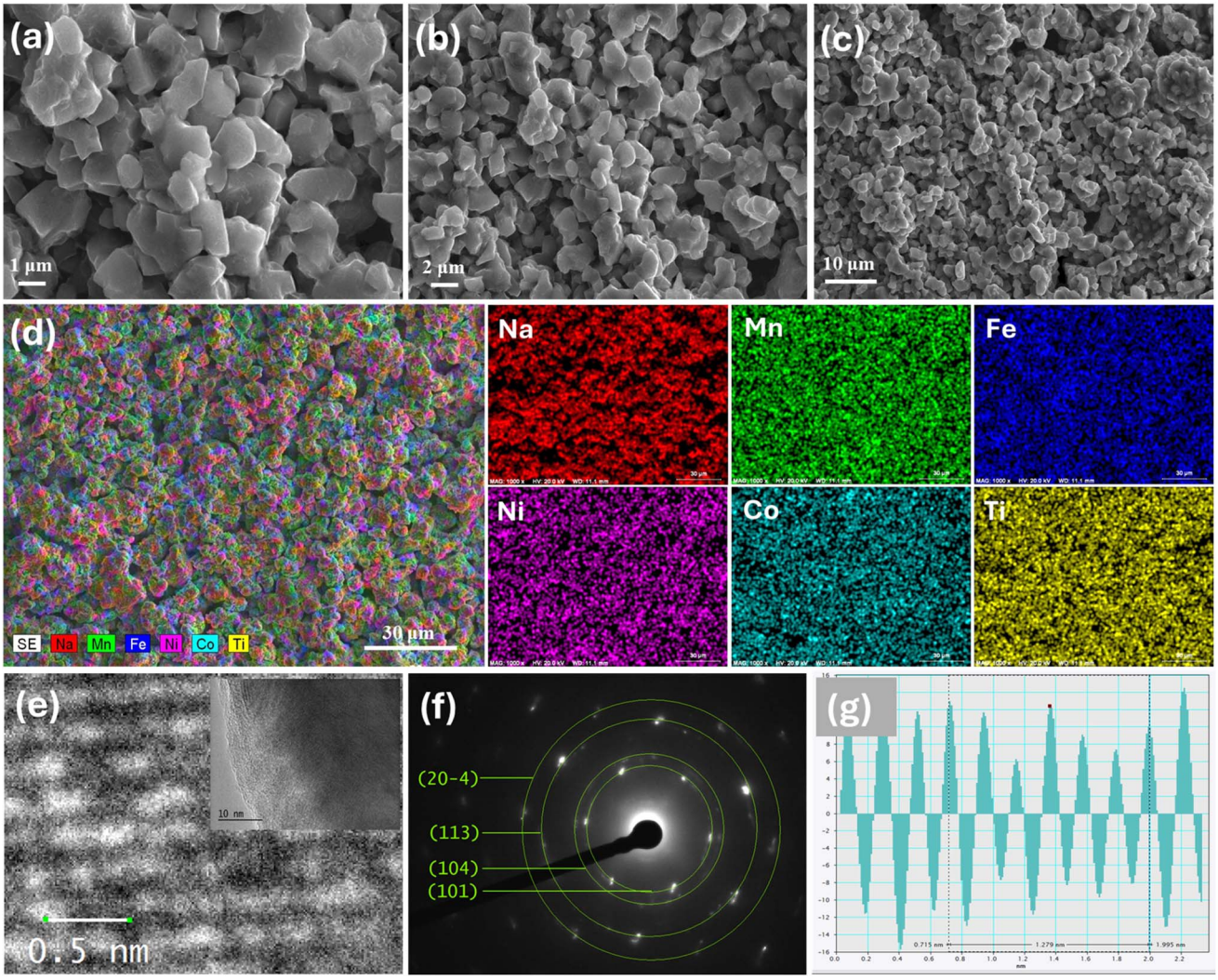

Fig. 2 Morphological and microstructural characterization of the synthesized HEO cathode. (a–c) Scanning electron microscopy (SEM) images at various magnifications, displaying the characteristic irregular plate-like particle morphology. (d) Corresponding EDX elemental mapping showing the homogeneous distribution of Na, Ti, Mn, Fe, Ni, and Co throughout the selected area. (e) Bright-field transmission electron microscopy (TEM) image revealing the particle microstructure. (f) Selected area electron diffraction (SAED) pattern confirming the high crystallinity and hexagonal symmetry of the P2-type phase. (g) High-resolution TEM (HR-TEM) image showing well-resolved lattice fringes and crystallographic reflection planes.

was carried out by dividing each elemental concentration by its respective atomic mass, followed by normalization. The calculated molar amounts were then normalized with respect to the total transition metal content to obtain the final stoichiometry. Upon converting these mass concentrations to molar ratios, the stoichiometry was calculated as $Na_{0.94}(Ti_{0.18}Mn_{0.20}Fe_{0.20}Ni_{0.21}Co_{0.21})O_2$. These results confirm that the measured composition is consistent with the intended high-entropy design. The Na/TM ratio determined by ICP is ~0.94, which is slightly lower than the theoretical unity; however, it is consistent with the expected sodium loss during high-temperature calcination.

The high-resolution transmission electron microscopy (HR-TEM) image in Fig. 2(e) of the synthesized HEO material provides visual evidence of its atomic-scale ordering. The low-magnification image in the inset further reveals the clean surface edges of the particles, where the layered ordering extends to the surface of the material.

The TEM image shows continuous lattice fringes without any detectable amorphous regions or grain boundaries, indicating the high crystallinity of the material. The lattice stripes with "black and white" contrast are a signature of the electron density distribution of the O3-type layered structure. The dark regions correspond to the transition metal oxide slabs containing cations with high atomic numbers that scatter electrons strongly. On the other hand, the bright regions represent sodium layers where the light Na^+ ions reside. The periodic and uniform nature of these layers suggests a coherent layered structure without phase separation or metal clustering in spite of the complexity of the composition containing five different TM. In addition, these bright sodium layers confirm the ICP-MS data, yielding a Na stoichiometry of ~0.94, which is a direct indication of an O3-type layered structure.

The selected area electron diffraction (SAED) analysis, shown in Fig. 2(f), exhibits well-defined spots forming concentric rings, indicating a polycrystalline structure of the selected region. The diffraction rings are indexed to the hexagonal setting of the $R\bar{3}m$ space group. The interplanar spacings (*d*-spacings) are calculated from the radii of the concentric rings and compared with the bulk structural information obtained from Rietveld refinement of the XRD data (Table 1). The consistency of these values, although one is obtained from local electron diffraction of a selected region and the other is obtained from the bulk XRD yielding the average structure, confirms that the high-entropy strategy successfully results in a single-phase solid solution with long-range structural order without any phase segregations. The interplanar spacings observed in the HR-TEM micrographs were calculated using a digital line profile analysis using the Gatan DigitalMicrograph software. Fig. 2(g) shows the intensity profile corresponding to the selected region in Fig. 2(e) (indicated by the green lines). In the periodic sinusoidal wave pattern, the peaks represent the high-density transition metal layers and the troughs correspond to the interlayer regions occupied by the light Na^+ ions. As shown in the profile, five consecutive lattice planes were measured to minimize the measurement error compared to measuring a single interlayer spacing, yielding a total distance of 1.279 nm. The average interlayer spacing is calculated as:

Table 1 Comparison of interplanar spacings (*d*-values) derived from SAED analysis and XRD refinement

Reflection plane	*d*-spacing (TEM) [nm]	*d*-spacing (XRD) [nm]
(101)	0.250	0.255
(104)	0.211	0.217
(113)	0.146	0.144
$(20\bar{4})$	0.122	0.123

$$d = \frac{1.279\ \text{nm}}{5} \approx 0.256\ \text{nm} \quad (2)$$

This value is in excellent agreement with that determined by Rietveld refinement for the *d*-spacing of the (101) crystallographic plane (0.255 nm), further indicating structural homogeneity.

Systematic XPS measurements were performed to determine the valence states of the $NaTi_{0.2}Mn_{0.2}Fe_{0.2}Ni_{0.2}Co_{0.2}O_2$ sample. The wide-scan survey spectrum of the as-synthesized sample shown in Fig. 3(a) confirms the presence of all constituent elements (Na, Ti, Mn, Fe, Ni, Co, and O) without detectable impurities. High-resolution core-level spectra were utilized to determine the local chemical environment of each TM. Table S1 lists the peak areas and the corresponding oxidation states of the elements, derived from the XPS spectra. The Ti 2p spectrum (Fig. 3(b)) shows a characteristic spin–orbit doublet with peaks observed at 457.98 eV (Ti $2p_{3/2}$) and 463.78 eV (Ti $2p_{1/2}$), confirming the presence of Ti^{4+} ions. The minor feature, observed at 453.79 eV, was assigned to a small Na Auger peak, which is usually visible in the presence of a high intensity Na 1s XPS signal.

The deconvoluted Mn 2p spectrum (Fig. 3(c)) shows a spin–orbit splitting into Mn $2p_{3/2}$ at 641.67 eV and Mn $2p_{1/2}$ at 653.11 eV. A satellite feature observed at 644.26 eV further supports the identified oxidation state of Mn^{3+}. The Fe 2p spectrum (Fig. 3(d)) reveals a complex structure with main peaks located at 711.15 eV (Fe $2p_{3/2}$) and 724.17 eV (Fe $2p_{1/2}$). The mixed valence states of Fe^{2+} and Fe^{3+} are evidenced by the satellite peaks at 718.41 eV and 732.73 eV, respectively.

The cobalt spectrum, shown in Fig. 3(e), was fitted with four distinct components. The peaks located at 779.76 eV and 795.18 eV are attributed to Co^{2+}, while the components at 781.19 eV and 796.95 eV correspond to the Co^{3+} state.[28,29] Finally, the Ni 2p spectrum shows two primary peaks at 854.98 eV (Ni $2p_{3/2}$) and 872.54 eV (Ni $2p_{1/2}$). The deconvolution of these peaks confirms a mixed Ni^{2+}/Ni^{3+} valence state, validated by the presence of satellite peaks at 861.5 eV and 879.75 eV. The deconvoluted high-resolution spectrum of C 1s (Fig. S4) clearly shows a dominant peak at 289.42 eV, which is the characteristic binding energy for inorganic Na_2CO_3, which could arise due to the interaction of Na with atmospheric CO_2. The peak at 290.70 eV is attributed to the presence of minor carbonate-related surface species, while the peak at 285.18 eV corresponds to adventitious carbon.

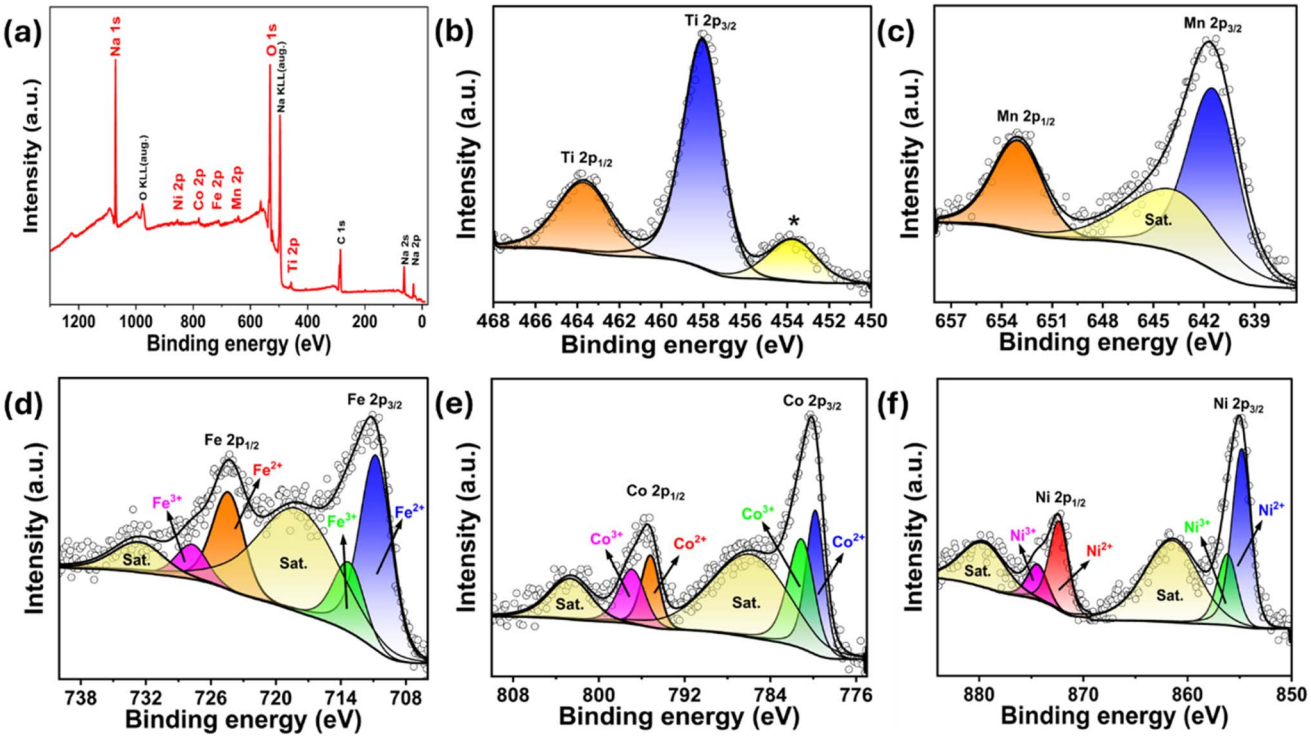

Fig. 3 Surface chemical state analysis of the HEO material. (a) XPS survey scan spectrum. (b–f) High-resolution spectra of Ti 2p, Mn 2p, Fe 2p, Co 2p, and Ni 2p regions.

3.2 Electrochemical performance of HEO cathodes

Fig. S5 shows the EIS analysis of HEO half cells, where the experimental Nyquist plots were fitted using the equivalent circuit model shown in the inset. The resulting fitting parameters are listed in Table S2. The series resistance (R_s), which corresponds to ohmic contributions from the electrolyte and contacts, was determined as 7.70 Ohms. The primary interface resistance (R_1) was calculated as 877 Ohms, with a constant phase element exponent (Q_{a1}) of 0.87, indicating non-ideal capacitive behavior characteristic of rough electrode surfaces. The second resistance element (R_2) was negligible (approximately 5.07×10^{-12} Ohms), suggesting that the secondary interface process did not significantly contribute to the impedance of this sample. The Warburg impedance (W), representing the solid-state diffusion of ions at low frequencies, was found to be 1.14×10^{-3} ohm $s^{-0.5}$. This parameter is directly related to the Na-ion diffusion coefficient and a lower Warburg coefficient typically indicates lower resistance to ion diffusion within the bulk electrode structure, facilitating faster kinetics during the charge/discharge process.

Fig. 4(a) shows the CV curves of HEO half cells at scan rates of 0.1, 0.2, 0.3, and 0.4 mV s^{-1}. The current density increases with the increasing scan rate. This is expected because the faster voltage sweep results in a higher flux of Na-ions to the electrode surface, requiring a larger current to accommodate the electrochemical reaction at higher speeds.

The Dunn method was used to calculate the contribution to charge storage from diffusion-controlled Faradaic reactions and surface-controlled capacitive/pseudocapacitive mechanisms, as shown in Fig. 4(b and c). Based on this method, the measured current at a given potential (i) consists of two components: a surface-controlled capacitive term proportional to the scan rate ($k_1 v$) and a diffusion-controlled term proportional to the square root of the scan rate ($k_2 v^{1/2}$), as described by eqn (3) and (4).[30–32]

$$i = k_1 v + k_2 v^{\frac{1}{2}} \quad (3)$$

$$\frac{i}{v^{\frac{1}{2}}} = k_1 v^{\frac{1}{2}} + k_2 \quad (4)$$

where "v" stands for the scan rate, and k_1 and k_2 represent the slope and intercept, respectively, of the $i/v^{1/2}$ *vs.* $v^{1/2}$ plot. The graphs verify that both surface-controlled capacitive and pseudocapacitive processes almost equally contribute to charge storage at 0.1 mV s^{-1}. An increase in overpotential reduces the diffusion contribution at higher scan rates.

Fig. 4(d) illustrates the rate capability of the $NaTi_{0.2}Mn_{0.2}Fe_{0.2}Ni_{0.2}Co_{0.2}O_2$ cathode in a half-cell configuration. At 0.1C (1C = 120 mA g^{-1}), the cell exhibited a high reversible specific capacity of approximately 146 mA h g^{-1}. As the current rate increases stepwise to 0.2, 0.5, 1, and 2C, the specific capacity decreases to 118, 104, 88, and 60 mA h g^{-1}, respectively. This capacity decay at high rates is attributed to the increased ohmic polarization and reduced Na-ion diffusion kinetics, which limit the full utilization of the active mass before reaching the voltage cutoff. Fig. 4(e) shows the galvanostatic charge–discharge voltage profiles of the HEO half-cell measured at a C/3 rate for

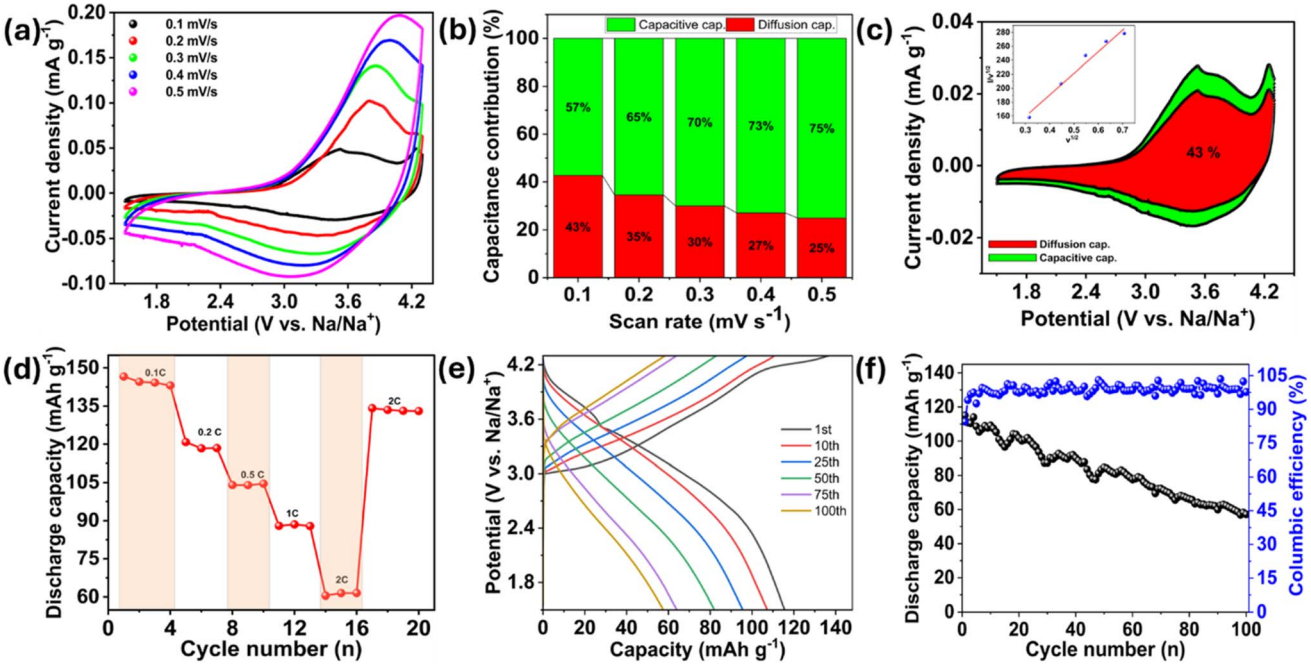

Fig. 4 (a) Cyclic voltammetry (CV) curves measured at scan rates ranging from 0.1 to 0.5 mV s^{-1} within a voltage window of 1.5–4.3 V; (b) quantitative analysis of the charge storage mechanism (diffusion-controlled *vs.* surface-capacitive) using the Dunn method; (c) CV profile at 0.1 mV s^{-1} showing the calculated capacitive contribution (shaded region) relative to the total current; (d) rate capability performance at various C-rates from 0.1C to 2C; (e) galvanostatic charge–discharge voltage profiles for the 1st, 10th, 25th, 50th, 75th, and 100th cycles; and (f) plot of capacity *vs.* cycle number with corresponding coulombic efficiency (CE%).

the 1st, 10th, 25th, 50th, 75th, and 100th cycles. In the first cycle, the cathode delivers a specific discharge capacity of ~118.4 mA h g^{-1} within the voltage window of 1.5 to 4.3 V. However, as the cycle number increases, there is a noticeable change in the voltage profiles, with the charge plateaus shifting to higher potentials while the discharge plateaus dropping to lower potentials. The widening of the voltage hysteresis is attributed to an increase in polarization and internal cell resistance over time. Fig. 4(f) shows the details of the cycling stability and corresponding coulombic efficiency over 100 cycles. Starting from an initial capacity of 118.4 mA h g^{-1}, the discharge capacity gradually decreases to 58.2 mA h g^{-1} by the 100th cycle, corresponding to a capacity retention of approximately 49%. Despite this low-capacity retention, the coulombic efficiency stabilizes after the initial cycles and remains at ~98% throughout the measurements, indicating reversible redox reactions. The observed capacity fade and increased polarization are attributed to slow kinetics. This increase in the impedance usually originates from surface degradation, such as the thickening of a resistive solid electrolyte interphase (SEI) layer or minor structural rearrangements at the cathode-electrolyte interface.

The initial discharge capacity of our HEO sample, ~118 mA h g^{-1} at C/3, shows a competitive result compared to the similar studies reported in the literature, as listed in Table 2. The higher initial capacities reported for sol–gel synthesized materials are attributed to the nano-sized particles and enhanced homogeneity. However, the solid state synthesis technique offers the advantage of industrial scalability and cost-effectiveness. In addition, our material outperforms several other solid-state synthesized HEOs because it does not involve any specific capacity-enhancing dopants like lithium (Li) or calcium (Ca) into the transition metal layer.[33,34] This suggests that the specific quinary combination of Ti-Mn-Fe-Ni-Co balances the redox potential and enhances structural stability through high configurational entropy.

Table 2 Comparison of HEO cathodes for sodium-ion batteries

Cathode material	Synthesis method	Test rate (C-rate)	Capacity (mAh g^{-1})	Capacity retention/cycles	Ref. no
$NaTi_{0.2}Mn_{0.2}Fe_{0.2}Ni_{0.2}Co_{0.2}O_2$	Solid-state reaction	C/3	~118	49.0%/100	This work
$Na_{0.9}Ca_{0.05}Fe_{0.2}Mn_{0.2}Ni_{0.2}Ti_{0.2}Li_{0.1}Co_{0.1}O_2$	Sol–gel method	0.1C	150	71.0%/200	35
$NaLi_{0.1}Ni_{0.3}Mn_{0.4}Fe_{0.1}Cu_{0.1}O_2$	Sol–gel method	0.2C	141	85.0%/1000	36
$Na_{0.83}Li_{0.1}Ni_{0.25}Co_{0.2}Mn_{0.15}Ti_{0.15}Sn_{0.15}O_2$	Solid-state reaction	0.1C	109.4	87.2%/200	37
$Na_{0.67}Ni_{0.3}Co_{0.015}Cu_{0.015}Fe_{0.015}Mn_{0.655}O_2$	Solid-state reaction	1C	113.2	85.7%/200	38
$Na_{0.67}[Mn_{0.4}Ni_{0.2}Fe_{0.1}Cu_{0.1}Zn_{0.05}Ti_{0.15}]O_2$	Solid-state reaction	0.1C	163	74.9%/500	39

4 Conclusions

Solid-state synthesis was utilized to produce the O3-type $NaTi_{0.2}Mn_{0.2}Fe_{0.2}Ni_{0.2}Co_{0.2}O_2$ cathode. We combined five transition metals to balance the redox activity of Co, Fe, and Ni with the structural support of Mn and Ti. The configurational entropy is determined as ~1.6 R, above the 1.5 R threshold, classifying our composition as a high-entropy oxide. Structural analysis *via* XRD and Rietveld refinement revealed a pure single phase hexagonal structure with *R*-3*m* symmetry. The calculated lattice parameters of $a = 2.9831(1)$ Å and $c = 16.071(1)$ Å were confirmed by HR-TEM and SAED, in which the visualized atomic ordering is extended to the particle surface. ICP and EDX studies provided consistent results for quantification of elements, which verifies the nominal composition. The mixed-valence states, identified *via* XPS analysis, reveal the charge-compensation mechanism active in the material. In sodium half-cell testing, the cathode showed a reversible discharge capacity of 118 mA h g^{-1} at a C/3 rate. Rate capability remained robust, with 60 mA h g^{-1} retained even at 2C. The kinetic behavior, studied using CV and the Dunn method, suggests that the charge storage mechanism is governed by capacitive effects due to the presence of interfacial resistance. In conclusion, this study verifies the stabilization of the O3-type structure through maximizing the configurational entropy. The multi-cation oxide with a pure single-phase provides favorable properties for sodium storage applications.

Conflicts of interest

There are no conflicts to declare.

Data availability

The data supporting the findings of this study are available from the corresponding author upon reasonable request.

Supplementary information (SI): additional figures and tables supporting the main findings of this study. See DOI: https://doi.org/10.1039/d6ra02449a.

Acknowledgements

The authors gratefully acknowledge the financial support provided by the Inonu University Scientific Research Projects Coordination Unit (Project ID: FYL-2025-4029). This research has also been supported by the NFFA project, which has received funding from the European Union's Horizon 2020 research and innovation program under grant agreement No. 101007417 (Proposal ID 1026).

References

1 K. Walczak, *et al.*, $NaMn_{0.2}Fe_{0.2}Co_{0.2}Ni_{0.2}Ti_{0.2}O_2$ high-entropy layered oxide-experimental and theoretical evidence of high electrochemical performance in sodium batteries, *Energy Storage Mater.*, 2022, **47**, 500–514, DOI: 10.1016/j.ensm.2022.02.038.

2 K. H. Tian, *et al.*, A three-in-one strategy of high-entropy, single-crystal, and biphasic approaches to design O3-type layered cathodes for sodium-ion batteries, *Energy Storage Mater.*, 2024, **73**, 103841, DOI: 10.1016/j.ensm.2024.103841.

3 X. Wan, *et al.*, High-Entropy Structural Modification Strategy for O3-type Layered Sodium-Ion Cathode Materials with Enhanced Electrochemical Performance, *ACS Appl. Energy Mater.*, 2025, **8**(10), 6451–6462, DOI: 10.1021/acsaem.5c00255.

4 X. Wang, *et al.*, High-entropy engineering enables O3-type layered oxide with high structural stability and reaction kinetic for sodium storage, *J. Colloid Interface Sci.*, 2025, **691**, 137438, DOI: 10.1016/j.jcis.2025.137438.

5 B. Xiao, *et al.*, Enhancing the electrochemical performance of O3-type high entropy layered oxide cathode for sodium-ion batteries via a covalent Co-(O-O) bonding, *Mater. Today Energy*, 2025, **51**, 101884, DOI: 10.1016/j.mtener.2025.101884.

6 Y. Xiao, *et al.*, A Stable Layered Oxide Cathode Material for High-Performance Sodium-Ion Battery, *Adv. Energy Mater.*, 2019, **9**(19), 1803978, DOI: 10.1002/aenm.201803978.

7 M. H. Han, *et al.*, A comprehensive review of sodium layered oxides: powerful cathodes for Na-ion batteries, *Energy Environ. Sci.*, 2015, **8**(1), 81–102, DOI: 10.1039/c4ee03192j.

8 X. Gao, *et al.*, Recent Advances for High-Entropy based Layered Cathodes for Sodium Ion Batteries, *Small Methods*, 2023, **7**(9), e2300152, DOI: 10.1002/smtd.202300152.

9 F. Ding, *et al.*, Using High-Entropy Configuration Strategy to Design Na-Ion Layered Oxide Cathodes with Superior Electrochemical Performance and Thermal Stability, *J. Am. Chem. Soc.*, 2022, **144**(18), 8286–8295, DOI: 10.1021/jacs.2c02353.

10 H. Hasegawa, *et al.*, Stabilized Phase Transition Process of Layered NaxCoO2via Ca-Substitution, 2021 via Ca-Substitution, *J. Electrochem. Soc.*, 2021, **168**(1), 010509, DOI: 10.1149/1945-7111/abd451.

11 Y. Y. Zhao, *et al.*, Progress of the Elements Doped $NaFeO_2$ Cathode Materials for High Performance Sodium-ion Batteries, *Chemistryselect*, 2021, **6**(36), 9701–9708, DOI: 10.1002/slct.202102304.

12 C. Zhang, *et al.*, Inhibition of phase transition in sodium-ion battery cathode material: From design to validation, *J. Alloys Compd.*, 2025, **1036**, 181798, DOI: 10.1016/j.jallcom.2025.181798.

13 W. Ko, *et al.*, Exceptionally increased reversible capacity of O3-type $NaCrO_2$ cathode by preventing irreversible phase transition, *Energy Storage Mater.*, 2022, **46**, 289–299, DOI: 10.1016/j.ensm.2022.01.023.

14 S. Y. An, *et al.*, Improving cycling performance of the NaNiO cathode in sodium-ion batteries by titanium substitution, *Future Mater.*, 2024, **3**(3), 035103, DOI: 10.1088/2752-5724/ad5faa.

15 K. Kubota, *et al.*, Impact of Mg and Ti doping in O3 type $NaNi_{1/2}Mn_{1/2}O_2$ on reversibility and phase transition during electrochemical Na intercalation, *J. Mater. Chem. A*, 2021, **9**(21), 12830–12844, DOI: 10.1039/d1ta01164b.

16 E. Grépin, *et al.*, Optimal Ti-substitution in layered oxide cathodes for Na-ion batteries, *Chem. Mater.*, 2024, **36**(21), 10804–10812, DOI: 10.1021/acs.chemmater.4c02501.
17 F. F. Gao, *et al.*, Ni/Fe Bimetallic Ions Co-Doped Manganese Dioxide Cathode Materials for Aqueous Zinc-Ion Batteries, *Batteries*, 2023, **9**(1), 50, DOI: 10.3390/batteries9010050.
18 S. Sen, *et al.*, High Entropy Oxides: Mapping the Landscape from Fundamentals to Future Vistas: Focus Review, *ACS Energy Lett.*, 2024, **9**(8), 3694–3718, DOI: 10.1021/acsenergylett.4c01129.
19 J. Zou, *et al.*, High-Entropy Oxides: Pioneering the Future of Multifunctional Materials, *ACS Nano*, 2024, **18**(51), 34492–34530, DOI: 10.1021/acsnano.4c12538.
20 Z. Wang, *et al.*, A Ni/Co-free high-entropy layered cathode with suppressed phase transition and near-zero strain for high-voltage sodium-ion batteries, *Chem. Eng. J.*, 2024, **480**, 148130, DOI: 10.1016/j.cej.2023.148130.
21 C. Zhao, *et al.*, High-Entropy Layered Oxide Cathodes for Sodium-Ion Batteries, *Angew Chem. Int. Ed. Engl.*, 2020, **59**(1), 264–269, DOI: 10.1002/anie.201912171.
22 B. H. Toby and R. B. Von Dreele, GSAS-II: the genesis of a modern open-source all purpose crystallography software package, *J. Appl. Crystallogr.*, 2013, **46**(2), 544–549, DOI: 10.1107/S0021889813003531.
23 X. Liang, *et al.*, High-energy and long-life O3-type layered cathode material for sodium-ion batteries, *Nat. Commun.*, 2025, **16**(1), 3505, DOI: 10.1038/s41467-025-58637-1.
24 R. D. Shannon, Revised effective ionic radii and systematic studies of interatomic distances in halides and chalcogenides, *Acta Crystallogr. A*, 1976, **32**(5), 751–767, DOI: 10.1107/s0567739476001551.
25 Z. P. Lin, S. L. Zhao and F. G. Wu, Structure and electrochemical properties of layered sodium manganese oxide Na_xMnO_2, *Mater. Res. Express*, 2019, **6**(9), 095509, DOI: 10.1088/2053-1591/ab2e4e.
26 C. Julien and G. A. Nazri, General Overview of Vibrational Spectroscopy of Layered Transition-Metal Oxides, *MRS Online Proc. Libr.*, 2011, **548**, 79, DOI: 10.1557/proc-548-79.
27 Z. Y. Cheng, *et al.*, Recent Advances in Enhancing Air Stability of Layered Oxide Cathodes for Sodium-Ion Batteries via High-Entropy Strategies, *Metals*, 2025, **15**(6), 646, DOI: 10.3390/met15060646.
28 M. C. Biesinger, *et al.*, Resolving surface chemical states in XPS analysis of first raw transition metals, oxide and hydroxides: Cr, Mn, Fe, Co and Ni, *Appl. Surf. Sci.*, 2011, **257**(7), 2717–2730, DOI: 10.1016/j.apsusc.2010.10.051.
29 R. X. Tang, Y. B. Chen and X. Y. Su, Effect of CoO substitution on the microwave dielectric properties of rock-salt structured $LiMg_6AlO_8$ ceramics, *J. Mater. Sci. Mater. Electron.*, 2026, **37**(6), 416, DOI: 10.1007/s10854-026-16665-7.
30 A. Naveed, *et al.*, Fabrication of quasi-solid-state hybrid supercapacitor using nanoarchitectured CNTs supported bismuth/iron bimetallic oxide composite as high-performance electrode material, *J. Power Sources*, 2025, **659**, 238379, DOI: 10.1016/j.jpowsour.2025.238379.
31 M. N. Hussain, *et al.*, Lanthanide (Er, Eu)-doped TiO_2 with enhanced kinetics for a high-performance asymmetric supercapacitor and oxygen evolution reaction, *ACS Appl. Eng. Mater.*, 2025, **3**(5), 1315–1326, DOI: 10.1016/j.jpowsour.2025.238379.
32 M. N. Hussain, *et al.*, Investigating the Impact of Ag Nanoparticles on N and S Co-Doped TiO_2 for Battery-Type Supercapacitor Application, *ChemistrySelect*, 2023, **8**(48), e202303224, DOI: 10.1002/slct.202303224.
33 M. C. Biesinger, *et al.*, Resolving surface chemical states in XPS analysis of first row transition metals, oxides and hydroxides: Cr, Mn, Fe, Co and Ni, *Appl. Surf. Sci.*, 2011, **257**(7), 2717–2730, DOI: 10.1016/j.apsusc.2010.10.051.
34 S. Hashimoto and A. Tanaka, Alteration of Ti 2p XPS spectrum for titanium oxide by low-energy Ar ion bombardment, *Surf. Interface Anal.*, 2002, **34**(1), 262–265, DOI: 10.1002/sia.1296.
35 Y. Chi, *et al.*, Exploration of High-Entropy Layered Oxides with Ultrahigh Rate Performance for Sodium-Ion Batteries, *ACS Appl. Mater. Interfaces*, 2025, **17**(50), 67802–67812, DOI: 10.1021/acsami.5c15732.
36 T. Cai, *et al.*, High-Entropy Layered Oxide Cathode Enabling High-Rate for Solid-State Sodium-Ion Batteries, *Nanomicro Lett.*, 2023, **16**(1), 10, DOI: 10.1007/s40820-023-01232-0.
37 H. Wang, *et al.*, High-Entropy Na-Deficient Layered Oxides for Sodium-Ion Batteries, *ACS Nano*, 2023, **17**(13), 12530–12543, DOI: 10.1021/acsnano.3c02290.
38 W. W. Yuan, *et al.*, Fully active high-entropy P2 layered-oxide cathode for high-energy-density and long-life sodium-ion battery, *Energy Storage Mater.*, 2026, **84**, 104810, DOI: 10.1016/j.ensm.2025.104810.
39 C. T. Chen, *et al.*, Stabilization of P2-type nickel manganese-based layered oxides via high-entropy doping and rapid calcination for long-cycle-life sodium-ion batteries, *J. Alloys Compd.*, 2025, **1040**, 183620, DOI: 10.1016/j.jallcom.2025.183620.